PAPER

Check for updates

Synthesis of graphene layers on polycrystalline Ni foil using liquid ethanol

Junhao Zhou,[a] Yefei Guo,[b] Elena Voloshina [ID] *[c] and Yuriy Dedkov [ID] *[d]

In our manuscript we demonstrate an easy and technologically relevant approach to the successful growth of monolayer and multilayer graphene layers on polycrystalline nickel (Ni-poly) substrates using liquid ethanol (C_2H_5OH) as a carbon precursor. The *ex situ* immersed in liquid ethanol Ni foils were subsequently *in situ* thermally annealed in UHV conditions. The graphene formation process and the layer's quality are analyzed using X-ray spectroscopy techniques (XPS and NEXAFS) as well as Raman spectroscopy, complemented by scanning electron microscopy for morphology assessment. This study demonstrates that graphene growth occurs through the decomposition of C_2H_5OH molecules at low annealing temperatures, partially releasing −OH and H_2O, followed by the formation of C−C dimers, which aggregate into graphene layers at high annealing temperatures. The role of nickel carbide (Ni_2C) during the graphene synthesis is also discussed. The obtained data provide precise insights into the graphene formation mechanisms giving information on the optimal synthesis temperature as well as on the layer thicknesses, quality, and electronic structure.

1 Introduction

Graphene is a two-dimensional material composed of carbon atoms arranged in a honeycomb lattice.[1,2] It exhibits exceptionally high electron and hole mobilities,[3,4] excellent visible light transmittance,[5] and remarkable mechanical stability.[6] Additionally, graphene demonstrates strong adhesion to various substrates. Since its discovery, it has attracted extensive attention for its potential applications across electronics, optics, heat management, and mechanics.[7–9] Graphene synthesis methods can be broadly categorized into mechanical exfoliation from highly oriented pyrolytic graphite, ultra-high vacuum pyrolysis of single-crystal SiC, chemical reduction of graphene oxide, and chemical vapour deposition (CVD), among others.[10]

The chemical vapour deposition (CVD) method involves the decomposition of carbon precursor gases, such as ethylene (C_2H_4), acetylene (C_2H_2), or methane (CH_4), on catalytically active metal substrates to promote graphene growth.[11–14] Nickel, particularly the Ni(111) surface, is widely used as a catalytic substrate due to its minimal lattice mismatch with graphene (less than 1%).[15–19] Both monolayer and multilayer graphene

can be grown on nickel substrates at relatively low temperatures (500–900 °C) *via* the CVD method.[12,18] Several factors influence graphene growth on polycrystalline metals, including surface pretreatment, hydrocarbon gas flow, and the use of additional gases such as Ar and H_2.[20,21] Moreover, in the nickel-catalyzed CVD graphene growth, the surface state, temperature, pressure, and heating and cooling rates of the nickel substrate significantly affect the resulting graphene layers.[22,23] Dahal *et al.*[18] demonstrated that temperature is the key factor governing graphene growth on nickel. Thiele *et al.*[24] investigated graphene growth on monocrystalline and polycrystalline nickel substrates, highlighting that smooth monocrystalline nickel surfaces favour the formation of single or bilayer graphene, while multilayer graphene tends to form at grain boundaries. Similarly, Zhang *et al.*[25] studied atmospheric pressure CVD growth on nickel, showing that single-layer graphene is formed on Ni(111) predominantly through a surface catalysis process, whereas graphene growth on polycrystalline nickel results from a combination of segregation and surface catalytic equilibrium. Further studies emphasized the role of the nickel carbide formed during graphene growth and its role at higher synthesis temperatures.[26–30]

In addition to hydrocarbon gases, other precursors such as gaseous ethanol and acetone have been demonstrated for graphene growth on metallic surfaces using high-temperature CVD.[31–33] Building on these findings, a new, faster, and more straightforward method for growing high-quality single-layer graphene on metallic substrates – specifically Ir(111) and Ru(0001) – from liquid ethanol was recently developed.[34] This approach follows earlier successful demonstrations of graphene

[a]Department of Physics, Shanghai University, 99 Shangda Road, 200444 Shanghai, P. R. China

[b]School of Physics and Advanced Energy, Henan University of Technology, Zhengzhou, 450000, Henan, P. R. China

[c]Division of Theoretical Physics, Ruđer Bošković Institute, Bijenička Cesta 54, 10000 Zagreb, Croatia. E-mail: elena.voloshina@irb.hr

[d]Center for Advanced Laser Techniques, Institute of Physics, Bijenička Cesta 46, 10000 Zagreb, Croatia. E-mail: ydedkov@ifs.hr

synthesis from liquid acetone precursors on Ir(111) and Rh(111).[35,36] The procedure involves immersing a freshly prepared metallic surface in liquid ethanol, followed by thermal annealing under ultra-high vacuum (UHV) conditions. An initial low-temperature annealing step at $T \approx 250\text{--}300\ ^\circ\text{C}$ is crucial, promoting the cleavage of ethanol molecules and the desorption of water from the metal surface. Subsequently, the remaining C_2H_2 molecules decompose at higher annealing temperatures, leading to carbon dimer aggregation into graphene fragments and eventually forming continuous layers. Ref. 34 demonstrated that the resulting graphene layers exhibit high quality, comparable to those produced *via* standard *in situ* CVD synthesis.[14,37] While previous studies focused on monocrystalline, well-ordered metallic surfaces, the goal of the present work is to adapt and evaluate this method for more practical substrates – specifically, polycrystalline nickel foil – which holds promise for scalable and high-yield graphene production.

In this work, we utilize liquid ethanol as a precursor for graphene growth on cost-effective polycrystalline nickel foil. The Ni substrate was first cleaned through cycles of Ar^+-ion sputtering and high-temperature annealing under UHV conditions. Following this, the substrate was *ex situ* immersed in liquid ethanol and subsequently subjected to stepwise annealing in an UHV. To monitor the graphene formation process and evaluate the quality of the resulting layers, we employed a range of characterization techniques, including X-ray photoelectron spectroscopy (XPS), near-edge X-ray absorption fine structure spectroscopy (NEXAFS), and scanning electron microscopy (SEM). Our findings show that ethanol molecules decompose under controlled thermal annealing, leading to the formation of C–C dimers, which aggregate into graphene fragments. This process is accompanied by the formation of Ni_2C, which also plays a role in the graphene conversion process. Spectroscopic analysis indicates that graphene layers on polycrystalline Ni foil form at temperatures around $T \approx 700\text{--}800\ ^\circ\text{C}$ when using liquid ethanol as a precursor – a range that may be advantageous for industrial applications. Additionally, we outline potential improvements for this easy and technologically relevant method to enhance the quality of the graphene layers grown on Ni polycrystalline foil.

2 Experimental details

The Ni substrate used in the present work is a 100 μm-thick Ni foil (purity > 99.99%). Before the experiment, it was ultrasonically cleaned using ethanol and deionized water successively ($T = 50\ ^\circ\text{C}$, $t = 30$ min) in order to remove contamination on the substrate surface before being placed in the UHV chamber. Then it was cleaned in UHV conditions using cycles of Ar^+ ion sputtering ($p(\text{Ar}) = 1 \times 10^{-5}$ mbar, $E_p = 1.5$ kV, $t = 60$ min) and thermal annealing ($T = 1000\ ^\circ\text{C}$, $t = 60$ min). The sample temperature in all experiments was measured using an infrared pyrometer. The cleanliness of the Ni polycrystalline substrate and the absence of any traces of C 1s and O 1s signals were monitored using XPS of the corresponding core levels.

Laboratory-based XPS experiments were performed in the experimental station for XPS/ARPES studies installed at the Shanghai University. This station consists of two chambers, preparation and analysis, with a base pressure better than 1×10^{-10} mbar (SPECS Surface Nano Analysis GmbH). The first one was equipped with standard preparation instruments allowing substrates preparation using Ar^+-ions sputtering and annealing, and with 4-grid LEED optics combined with a CCD-camera for sample structural characterization. XPS spectra were measured using a monochromatized Al K_α ($h\nu = 1486.6$ eV) X-ray source FOCUS 500 and SPECS PHOIBOS 150 hemispherical analyzer combined with a 2D-CMOS detector.

Synchrotron-based XPS and NEXAFS experiments were performed at the EA01 endstation of the SMS branch of the FlexPES beamline (MAX IV synchrotron radiation facility, Lund, Sweden).[38] Here, all spectra were measured in UHV conditions (base vacuum is below 1×10^{-10} mbar) and at room temperature. NEXAFS spectra were collected with the partial electron yield (PEY) detector with a grid repulsive voltage of $U = -150$ V. XPS spectra were acquired using a Scienta Omicron DA30-L(W) energy analyzer.

SEM images were collected *ex situ* after XPS experiments using a JSM-IT800 equipped with JEOL In-lens Schottky Plus field emission electron gun.

Raman spectra of the samples were collected *ex situ* after the final annealing step at $T = 1000\ ^\circ\text{C}$ using a Renishaw inVia Qontor. Samples were illuminated with a laser of wavelength of 532 nm and a power of 100 mW with a 1 μm laser spot. Before characterization, a standard monocrystalline Si wafer was used to calibrate the system.

3 Results and discussion

The experimental procedure for synthesizing graphene layers on polycrystalline Ni foil is illustrated in Fig. 1 (for a detailed description of the experimental details, see SI). Initially, the Ni foil is pre-cleaned in air using ethanol and deionized water, then loaded into an UHV chamber, where it undergoes cycles of Ar^+-ion sputtering and high-temperature annealing. The results of this UHV-based cleaning process are shown in Fig. S1 of the SI. XPS spectra of the "as-loaded" Ni foil reveal strong O 1s and C 1s emission lines, indicating significant surface
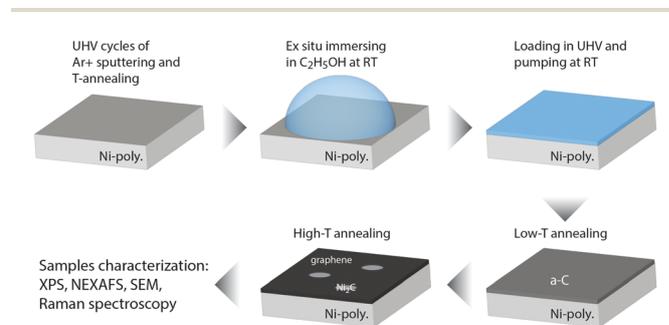

Fig. 1 Experimental scheme used in this study for graphene synthesis on polycrystalline Ni polycrystalline foil from a liquid ethanol precursor.

contamination. After multiple cleaning cycles involving Ar^+-ion sputtering and thermal annealing at $T = 1000$ °C, an atomically clean Ni surface is achieved. This is confirmed by the disappearance of the contamination-related emission lines and a notable increase in Ni 2p and valence band emission signals, characteristic of a clean metallic surface.

After UHV cleaning, the Ni foil is removed from the vacuum chamber and immersed in liquid ethanol for 30 seconds, under a slow nitrogen gas flow to minimize surface contamination. The foil is then quickly transferred to the load-lock chamber, where it is evacuated to a vacuum level of 5×10^{-8} mbar. The total time the ethanol/Ni system spends in air is kept to a maximum of approximately 60 seconds. Following this, the Ni foil with the thick ethanol layer is introduced into the UHV preparation chamber, where stepwise thermal annealing (both low- and high-temperature) with an approximate rate of 10° per minute and the corresponding spectroscopic experiments are conducted.

Before discussing the spectroscopic results, a series of SEM images of the system obtained after ethanol deposition on Ni foil and subsequent high-temperature annealing at 1000 °C are presented in Fig. 2. Since the surface of the Ni foil was initially covered by a thick ethanol film, and the system was then annealed at high temperature, we expect the Ni surface to be completely covered with monolayer or multilayer graphene by the end of the process. The observed contrast in the SEM images is therefore due to variations in the thickness of the graphene layers on the Ni foil. As previously demonstrated,[39] the charge transfer from the metal to graphene layers with different thicknesses varies, resulting in different work function values and hence colour contrast differences in the SEM images. The

non-uniformity in graphene coverage is clearly visible in the SEM images (Fig. 2), with lighter or brighter areas corresponding to regions with thinner graphene or lower work functions, and darker areas representing regions with more graphene layers. Based on these observations (and further discussed below), it can be concluded that the high-temperature annealing predominantly results in multilayer graphene coverage on the Ni foil, with the fraction of monolayer graphene not exceeding 10–15%. Additionally, prolonged thermal annealing leads to the formation of a carbidic phase (Ni_2C) at the surface, with several fragments likely identifiable in the SEM images (see Fig. 2, top-right image). The respective Raman spectra collected *ex situ* for different places on the graphene/Ni-foil sample (after the final annealing steps at $T = 1000$ °C) are presented in Fig. 3. As expected, the corresponding Raman spectrum of multilayer graphene shows two intense Raman features, which are assigned to G (≈ 1584 cm^{-1}) and 2D (≈ 2670 cm^{-1}) peaks. Also observed are strong D (≈ 1337 cm^{-1}) and D′ (≈ 1624 cm^{-1}) peaks, which are activated by defects such as in-plane heteroatom substitutions, vacancies, or grain boundaries.[40,41] Along with that, no Raman graphene-related peaks are found for the sample's places assigned to the Ni_2C fragments.

The detailed information on the ethanol decomposition and the formation of a graphene layer on Ni polycrystalline foil was obtained through a series of XPS and NEXAFS experiments, the results of which are compiled in Fig. 4 and 5. Both figures present the respective spectra collected after the corresponding annealing steps of the ethanol/Ni-poly system. Previous studies have provided detailed insight into the adsorption and decomposition behavior of ethanol molecules on transition-metal surfaces. On Pt(111), a submonolayer (0.44 ML) of
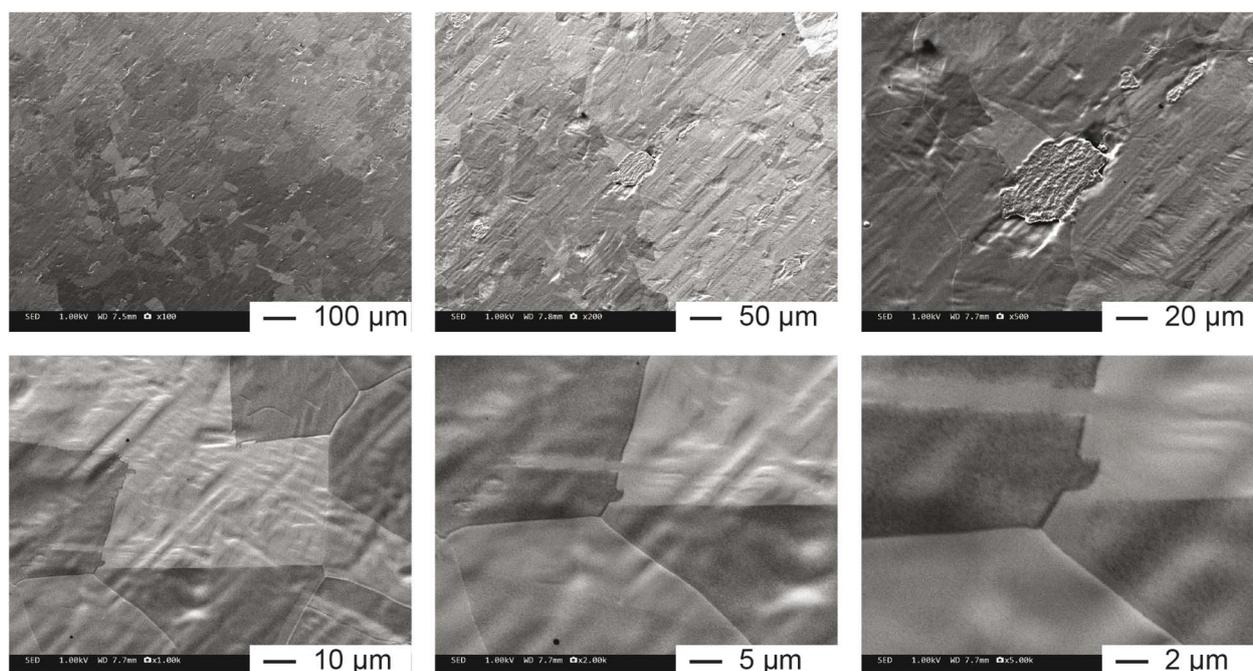

Fig. 2 Series of SEM images taken after the final annealing step at $T = 1000$ °C of the thick ethanol layer on Ni polycrystalline foil. Scale bars are provided for each image.
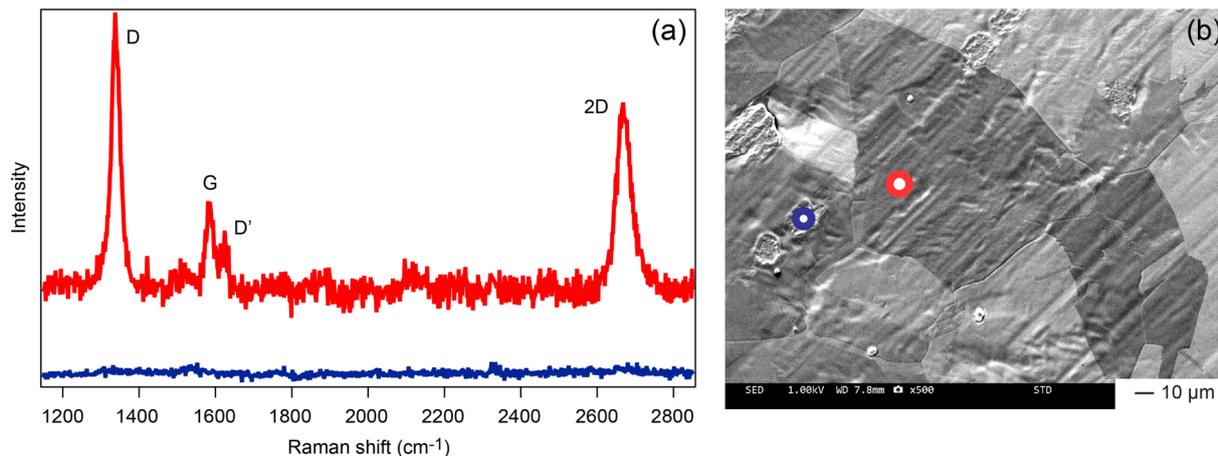
Fig. 3 Raman spectra (a) collected at different places of the graphene/Ni–poly sample marked by the circle of the respective color in the SEM image (b).

ethanol molecules adsorbed at 100 K undergoes stepwise dehydrogenation through an acetyl intermediate, yielding CO and CH_4 upon heating,[42] while on Cu surfaces, molecular ethanol first forms stable ethoxy species that dehydrogenate into acetaldehyde without complete dissociation.[43] In contrast, Ni surfaces exhibit much higher catalytic activity, where ethanol rapidly decomposes *via* α–C–H bond cleavage to produce CH_4, CO, and surface carbide species such as Ni_2C.[44] These results demonstrate that Ni favours deep dehydrogenation and carbide formation, processes that are directly relevant to the ethanol-assisted graphene growth investigated in this work.

In our experiments, after *ex situ* rinsing of the Ni poly-crystalline foil in liquid ethanol, distinct XPS signals attributed to carbon and oxygen atoms are observed ("RT", room temperature) (Fig. 4(a–c)). Meanwhile, the intensities of the Ni 2p XPS peaks are significantly reduced (*cf.* Fig. 4(d) and S1 of the SI) due to the attenuation of the photoemission signal from the substrate caused by the thick ethanol film. The corresponding "RT" C 1s spectrum (Fig. 4(c)) shows two photoemission peaks at 289.3 eV and 285.91 eV, which can be assigned to ethanol molecules directly in contact with the surface of the Ni foil and to the thick layer of C_2H_5OH molecules on top, respectively. A similar pattern was observed for a thick ethanol film on Ir(111),[34] although the peaks were located at slightly lower binding energies due to the weaker interaction between C_2H_5OH and Ir compared to the Ni surface. In addition, the O 1s XPS spectrum of the thick ethanol film on Ni foil reveals two emission components at 529.87 eV and 532.09 eV, which can be attributed to the oxidation of the Ni surface[45,46] and to the thick layer of ethanol molecules on top,[47] respectively.

The C K-edge NEXAFS spectrum of the thick ethanol film on Ni foil (bottom spectrum in Fig. 5) reveals several pronounced features that can be assigned to C $1s \rightarrow \pi^*_{C-C}$ at 285.02 eV, C $1s \rightarrow \pi^*_{C-O}$ at 288.22 eV, C $1s \rightarrow \sigma^*_{C-C}$ at 292.27 eV, and a broad shoulder for C $1s \rightarrow \sigma^*_{C-O}$ above 297 eV.[48–50] The observed difference between normal incidence (NI) and normal emission (NE) spectra, however, is not very pronounced due to the

absence of a preferential orientation of the C_2H_5OH molecules in the thick ethanol film on Ni foil.

The first annealing step at $T = 250$ °C of the thick ethanol film on Ni foil leads to dramatic changes in the XPS and NEXAFS spectra (see Fig. 4 and 5). First, the previously observed strong O 1s emission becomes much less prominent, showing a reduction in total intensity by a factor of ≈ 10 (both peak- and integral-intensity values), while the intensity of the Ni 2p line significantly increases. The binding energy of this O 1s line remains unchanged after this low-temperature annealing. At the same time, the integral intensity of the C 1s peak is reduced by a factor of 1.4, with a shift of this line (accompanied by a small shoulder on the right-hand side) to lower binding energies by ≈ 0.6 eV. A similar conclusion can be drawn from the analysis of the respective NEXAFS spectra, where the intensity of the C $1s \rightarrow \pi^*_{C-O}$ feature is significantly reduced (second spectrum from the bottom in Fig. 5). These observations indicate that this low-temperature (250 °C) annealing step is crucial for the cleavage of the ethanol molecules, partially removing –OH and H_2O, and leaving carbon-based fragments on the surface of the Ni foil. A similar observation has been made in several previous studies on the decomposition of oxygen-containing liquid precursors used for the synthesis of graphene on metallic surfaces.[34–36] However, compared to previously studied systems, where 4d- or 5d-metals were immersed in liquid ethanol, the ethanol/Ni-foil system demonstrates the presence of oxygen even after the first annealing step (as well as after the next two at higher annealing temperatures), suggesting a stronger interaction between the surface of the Ni polycrystalline foil and the ethanol molecules, as well as the resulting carbon-based fragments. Such an interaction might also lead to the slight oxidation of the surface Ni atoms of the metallic foil as manifested by the presence of the weak O 1s peak, which disappears at higher annealing temperatures (see discussion below).

Further annealing steps at $T = 400$ °C and $T = 600$ °C lead to a continuous reduction in the oxygen concentration in the studied system, accompanied by the gradual shift of the C 1s
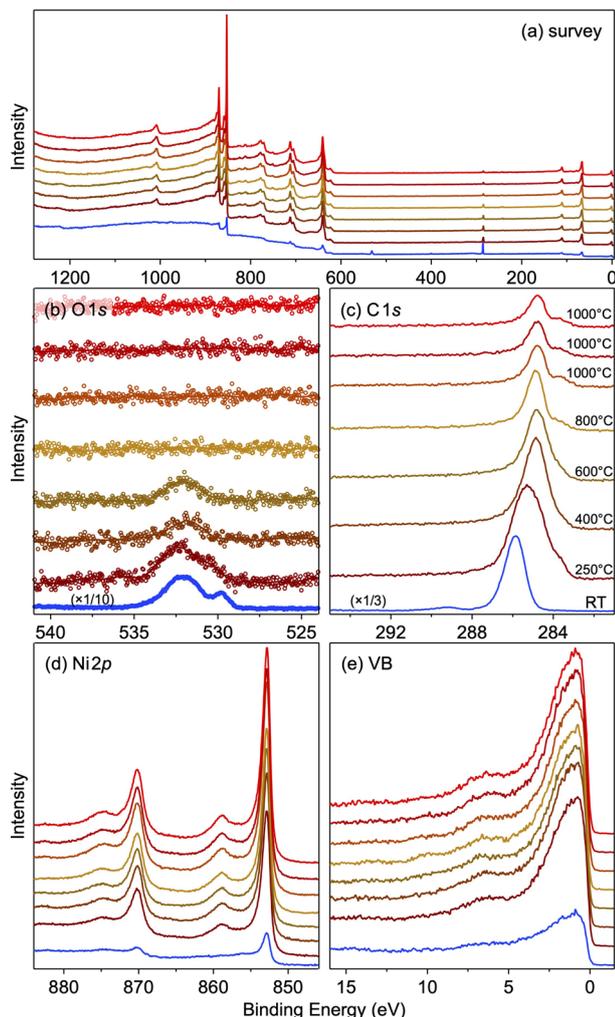
Fig. 4 XPS spectra collected after each annealing step of the thick ethanol layer on Ni polycrystalline foil: (a) survey, (b) O 1s, (c) C 1s, (d) Ni 2p, (e) valence band. Photon energy used in the experiment is $h\nu = 1486.6$ eV (Al K_α). Annealing temperatures, marked in panel (c), increase from bottom to top in each panel. Each annealing step lasted for 30 minutes. Last three spectra in every panel were collected after similar annealing at $T = 1000$ °C.

Fig. 5 Series of C K NEXAFS spectra collected after each annealing step of the thick ethanol layer on Ni polycrystalline foil. Annealing temperatures are indicated for each absorption spectrum. Each annealing step lasted 30 minutes. Normal incidence (NI) and normal emission (NE) correspond to the angles between the direction of the linear polarization of the incoming light and the normal to the sample's surface of $\alpha = 90°$ and $\alpha = 48°$, respectively.

peak to lower binding energies of 284.86 eV and 284.81 eV, respectively (Fig. 4). In parallel, the corresponding NEXAFS spectra show significant transformation of the respective X-ray absorption features, with the formation of graphene-related C 1s$\rightarrow\pi^*_{\text{C-C}}$ and C 1s$\rightarrow\sigma^*_{\text{C-C}}$ features at ≈ 285.3 eV and ≈ 292.1 eV, respectively, being promoted during these annealing steps (Fig. 5).

The annealing of the studied system at $T = 800$ °C leads to the formation of ordered graphene layers on top of the Ni polycrystalline foil. This is evidenced by the complete desorption of oxygen, as indicated by the absence of the respective O 1s XPS spectra, as well as by the narrowing of the C 1s spectrum, which suggests the structural uniformity of the carbon layer on the Ni foil (Fig. 4). However, the extracted value for the FWHM (full width at half maximum) of the C 1s line measured after this annealing step is 0.99 eV, indicating the multicomponent
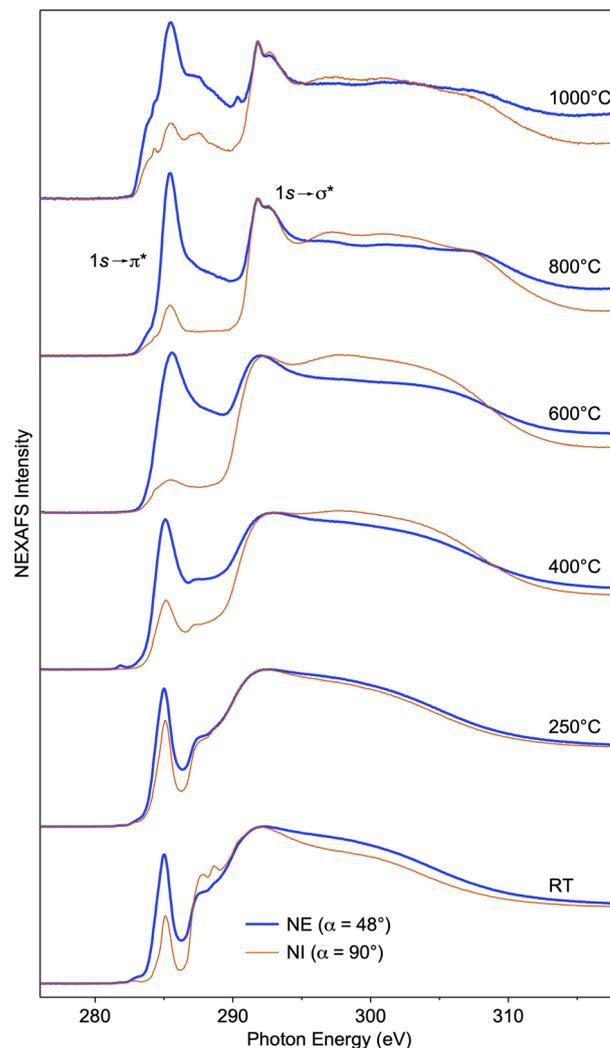
nature of this line. This corresponds to formation of single- and multilayer graphene on the Ni foil, which supports our conclusions from the SEM experiments on this system. At the same time, the formation of Ni_2C is observed, as revealed by the well-developed shoulder located at ≈ 283.7 eV in the C 1s spectrum.[51,52]

The formation of predominantly multi-layer graphene coverage on the Ni polycrystalline foil after the annealing step at $T = 800$ °C is also confirmed by the respective C K NEXAFS spectrum (Fig. 5). First, the well-pronounced C 1s$\rightarrow\pi^*_{\text{C-C}}$ and C 1s$\rightarrow\sigma^*_{\text{C-C}}$ sharp features at 285.42 eV and 291.82 eV, respectively, are observed, indicating the high structural ordering of the graphene layer on the Ni foil. Second, the representative double-peak structure for the C 1s$\rightarrow\sigma^*_{\text{C-C}}$ transition is observed, again pointing to the formation of well-ordered

graphene layers.[53–55] The respective energy difference between the above-described graphene-related transitions is 6.4 eV, which is very close to the value observed for free-standing graphene as well as the value obtained from calculations,[55,56] and differs from the reduced value for this energy difference characteristic of the 1 ML-thick graphene/Ni(111) interface.[57,58] As noted earlier, the formation of Ni_2C can also be identified in the NEXAFS spectrum as the shoulder observed on the low-energy side of the C 1s→π^*_{C-C} peak at 283.8 eV, which also correlates with the respective XPS data for this system.

As can be seen, the pronounced annealing of the formed graphene layers on the Ni foil at $T = 1000$ °C leads to the intensive dissolution of carbon atoms in the Ni polycrystalline foil, resulting in the subsequent formation of a significant Ni_2C fraction in the studied samples. This can be deduced from the respective C 1s XPS and C K NEXAFS spectra collected after three consecutive annealing steps at the same temperature of $T = 1000$ °C, indicating the steady state in the C–Ni system. Thus, the optimal temperature range for the formation of graphene layers on Ni polycrystalline foil spans 700–800 °C. Here, the role of Ni_2C at different annealing temperatures can be considered multifaceted. At low annealing temperatures (<700–800 °C), the formed Ni_2C randomly distributed in islands may act as a dynamic carbon reservoir, releasing carbon atoms during annealing and providing localized carbon sources for graphene growth (i.e., at these conditions Ni_2C can be considered as an intermediate product). At high annealing temperatures (>700–800 °C), under fixed carbon supply conditions (fixed volume of the ethanol drop, as in the present experiment), this leads to carbon starvation, resulting in reduced graphene domain sizes and the formation of voids on the sample's surface. Consequently, the high-temperature annealing process at $T = 1000$ °C not only fails to enhance the quality of the graphene layer but also interferes with the growth process. Thus, at high annealing temperatures, Ni_2C can be considered as a byproduct of graphene growth on Ni foil. This supports the conclusion about the optimal synthesis temperature for the graphene growth on the Ni polycrystalline foil. However, further intensive studies in this direction are required that will lead to the synthesis of high quality graphene layers on polycrystalline metallic supports using liquid precursors.[59]

4 Conclusions

In conclusion, we demonstrated that multilayer graphene can be easily and quickly synthesized on Ni polycrystalline foil from a liquid ethanol precursor. It was found that low-temperature annealing is an essential step, leading to the cleavage of C_2H_5OH molecules, followed by the partial removal of –OH and H_2O from the system. Further annealing steps lead to the transformation of carbon fragments and carbon dimers into graphene mono- and multi-layers, as deduced from the XPS, NEXAFS, and SEM analyses. It is found that the optimal temperature for graphene synthesis on Ni foil is in the range of 700–800 °C, which can be easily adopted in various technological processes, where graphene layers can be synthesized from the inexpensive precursor and subsequently transferred to the desired support for further practical applications.

Conflicts of interest

There are no conflicts to declare.

Data availability

All data supporting this article have been presented within the main text.

Supplementary information is available. See DOI: https://doi.org/10.1039/d5ra06724c.

Notes and references

1 A. K. Geim and K. S. Novoselov, *Nat. Mater.*, 2007, **6**, 183–191.
2 A. K. Geim, *Science*, 2009, **324**, 1530–1534.
3 K. Bolotin, K. Sikes, Z. Jiang, M. Klima, G. Fudenberg, J. Hone, P. Kim and H. Stormer, *Solid State Commun.*, 2008, **146**, 351–355.
4 K. S. Kim, Y. Zhao, H. Jang, S. Y. Lee, J. M. Kim, K. S. Kim, J.-H. Ahn, P. Kim, J.-Y. Choi and B. H. Hong, *Nature*, 2009, **457**, 706–710.
5 R. R. Nair, P. Blake, A. N. Grigorenko, K. S. Novoselov, T. J. Booth, T. Stauber, N. M. R. Peres and A. K. Geim, *Science*, 2008, **320**, 1308.
6 C. Lee, X. Wei, J. W. Kysar and J. Hone, *Science*, 2008, **321**, 385–388.
7 Y. Gao, T. Cao, F. Cellini, C. Berger, W. A. d. Heer, E. Tosatti, E. Riedo and A. Bongiorno, *Nat. Nanotechnol.*, 2018, **13**, 133–138.
8 F. Schwierz, *Nat. Nanotechnol.*, 2010, **5**, 487–496.
9 G. Zhao, X. Li, M. Huang, Z. Zhen, Y. Zhong, Q. Chen, X. Zhao, Y. He, R. Hu, T. Yang, R. Zhang, C. Li, J. Kong, J.-B. Xu, R. S. Ruoff and H. Zhu, *Chem. Soc. Rev.*, 2017, **46**, 4417–4449.

10 V. B. Mbayachi, E. Ndayiragije, T. Sammani, S. Taj, E. R. Mbuta and A. u. khan, *Results Chem.*, 2021, **3**, 100163.

11 J. Wintterlin and M.-L. Bocquet, *Surf. Sci.*, 2009, **603**, 1841–1852.

12 C.-C. Lu, C. Jin, Y.-C. Lin, C.-R. Huang, K. Suenaga and P.-W. Chiu, *Langmuir*, 2011, **27**, 13748–13753.

13 M. Batzill, *Surf. Sci. Rep.*, 2012, **67**, 83–115.

14 Y. Dedkov and E. Voloshina, *J. Phys.: Condens. Matter*, 2015, **27**, 303002.

15 M. Eizenberg and J. Blakely, *Surf. Sci.*, 1979, **82**, 228–236.

16 M. Eizenberg and J. M. Blakely, *J. Chem. Phys.*, 1979, **71**, 3467–3477.

17 Y. S. Dedkov, M. Fonin and C. Laubschat, *Appl. Phys. Lett.*, 2008, **92**, 052506.

18 A. Dahal and M. Batzill, *Nanoscale*, 2014, **6**, 2548–2562.

19 D.-M. Xie, Q.-F. Zou, D.-M. Zhu, T.-Y. Yang, X.-M. Zhang and X.-L. Li, *Diamond Relat. Mater.*, 2022, **129**, 109357.

20 N. Liu, L. Fu, B. Dai, K. Yan, X. Liu, R. Zhao, Y. Zhang and Z. Liu, *Nano Lett.*, 2011, **11**, 297–303.

21 Z. Ye, K. Xu, Q. Li, S. Lu, H. Wang, J. Zhao, L. Chen, F. Zeng, P. Ding, X. Tian and Y. Du, *J. Exp. Nanosci.*, 2023, **18**, 1–13.

22 Y. Chen, J. Wang, P. Schützendübe, Z. Wang and E. J. Mittemeijer, *Carbon*, 2020, **159**, 37–44.

23 F. Akhtar, J. Dabrowski, M. Lisker, P. Zaumseil, S. Schulze, A. Jouvray, P. Caban, A. Mai, C. Wenger and M. Lukosius, *Thin Solid Films*, 2019, **690**, 137565.

24 S. Thiele, A. Reina, P. Healey, J. Kedzierski, P. Wyatt, P.-L. Hsu, C. Keast, J. Schaefer and J. Kong, *Nanotechnology*, 2010, **21**, 015601.

25 Y. Zhang, T. Gao, S. Xie, B. Dai, L. Fu, Y. Gao, Y. Chen, M. Liu and Z. Liu, *Nano Res.*, 2012, **5**, 402–411.

26 B. C. Bayer, D. A. Bosworth, F. B. Michaelis, R. Blume, G. Habler, R. Abart, R. S. Weatherup, P. R. Kidambi, J. J. Baumberg, A. Knop-Gericke, R. Schloegl, C. Baehtz, Z. H. Barber, J. C. Meyer and S. Hofmann, *J. Phys. Chem. C*, 2016, **120**, 22571–22584.

27 L. L. Patera, C. Africh, R. S. Weatherup, R. Blume, S. Bhardwaj, C. Castellarin-Cudia, A. Knop-Gericke, R. Schloegl, G. Comelli, S. Hofmann and C. Cepek, *ACS Nano*, 2013, **7**, 7901–7912.

28 L. L. Patera, F. Bianchini, C. Africh, C. Dri, G. Soldano, M. M. Mariscal, M. Peressi and G. Comelli, *Science*, 2018, **359**, 1243–1246.

29 R. S. Weatherup, H. Amara, R. Blume, B. Dlubak, B. C. Bayer, M. Diarra, M. Bahri, A. Cabrero-Vilatela, S. Caneva, P. R. Kidambi, M.-B. Martin, C. Deranlot, P. Seneor, R. Schloegl, F. Ducastelle, C. Bichara and S. Hofmann, *J. Am. Chem. Soc.*, 2014, **136**, 13698–13708.

30 R. S. Weatherup, B. C. Bayer, R. Blume, C. Baehtz, P. R. Kidambi, M. Fouquet, C. T. Wirth, R. Schlogl and S. Hofmann, *ChemPhysChem*, 2012, **13**, 2544–2549.

31 A. Gnisci, G. Faggio, G. Messina, J. Kwon, J.-Y. Lee, G.-H. Lee, T. Dikonimos, N. Lisi and A. Capasso, *J. Phys. Chem. C*, 2018, **122**, 28830–28838.

32 A. K. Singh and A. K. Gupta, *IOP Conf. Ser.: Mater. Sci. Eng.*, 2018, **360**, 012012.

33 R. Brajpuriya, *J. Mater. Res.*, 2021, **36**, 3258–3266.

34 Y. Dedkov, J. Zhou, Y. Guo and E. Voloshina, *Adv. Mater. Interfaces*, 2023, **10**, 2300468.

35 F. Müller, H. Sachdev, S. Hüfner, A. J. Pollard, E. W. Perkins, J. C. Russell, P. H. Beton, S. Gsell, M. Fischer, M. Schreck and B. Stritzker, *Small*, 2009, **5**, 2291–2296.

36 F. Müller, S. Grandthyll, C. Zeitz, K. Jacobs, S. Hüfner, S. Gsell and M. Schreck, *Phys. Rev. B: Condens. Matter Mater. Phys.*, 2011, **84**, 075472.

37 Y. Dedkov, E. Voloshina and M. Fonin, *Phys. Status Solidi B*, 2015, **252**, 451–468.

38 A. Preobrajenski, A. Generalov, G. Öhrwall, M. Tchaplyguine, H. Tarawneh, S. Appelfeller, E. Frampton and N. Walsh, *J. Synchrotron Radiat.*, 2023, **30**, 831–840.

39 K. Takahashi, K. Yamada, H. Kato, H. Hibino and Y. Homma, *Surf. Sci.*, 2012, **606**, 728–732.

40 Y. Liu, Z. Liu, W. S. Lew and Q. J. Wang, *Nanoscale Res. Lett.*, 2013, **8**, 335.

41 C. Su, M. Tripathi, Q.-B. Yan, Z. Wang, Z. Zhang, C. Hofer, H. Wang, L. Basile, G. Su, M. Dong, J. C. Meyer, J. Kotakoski, J. Kong, J.-C. Idrobo, T. Susi and J. Li, *Sci. Adv.*, 2019, **5**, eaav2252.

42 A. F. Lee, D. E. Gawthrope, N. J. Hart and K. Wilson, *Surf. Sci.*, 2004, **548**, 200–208.

43 M. Bowker and R. Madix, *Surf. Sci.*, 1982, **116**, 549–572.

44 T. Kratochwil, M. Wittmann and J. Küppers, *J. Electron Spectrosc. Relat. Phenom.*, 1993, **64**, 609–617.

45 S. Uhlenbrock, C. Scharfschwerdt, M. Neumann, G. Illing and H. J. Freund, *J. Phys.: Condens. Matter*, 1992, **4**, 7973.

46 B. Payne, M. Biesinger and N. McIntyre, *J. Electron Spectrosc. Relat. Phenom.*, 2012, **185**, 159–166.

47 Y. Zhang, A. Savara and D. R. Mullins, *J. Phys. Chem. C*, 2017, **121**, 23436–23445.

48 W. E. S. Unger, A. Lippitz, C. Wöll and W. Heckmann, *Fresenius' J. Anal. Chem.*, 1997, **358**, 89–92.

49 M. Brzhezinskaya, V. Morilova, E. Baitinger, S. Evsyukov and L. Pesin, *Polym. Degrad. Stab.*, 2014, **99**, 176–179.

50 C. A. d. S. Moura, G. K. Belmonte, P. G. Reddy, K. E. Gonslaves and D. E. Weibel, *RSC Adv.*, 2018, **8**, 10930–10938.

51 R. Rameshan, L. Mayr, B. Klotzer, D. Eder, A. Knop-Gericke, M. Havecker, R. Blume, R. Schlogl, D. Y. Zemlyanov and S. Penner, *J. Phys. Chem. C*, 2015, **119**, 26948–26958.

52 C. Africh, C. Cepek, L. L. Patera, G. Zamborlini, P. Genoni, T. O. Menteş, A. Sala, A. Locatelli and G. Comelli, *Sci. Rep.*, 2016, **6**, 19734.

53 P. A. Bruhwiler, A. J. Maxwell, C. Puglia, A. Nilsson, S. Andersson and N. Martensson, *Phys. Rev. Lett.*, 1995, **74**, 614–617.

54 O. Wessely, M. I. Katsnelson and O. Eriksson, *Phys. Rev. Lett.*, 2005, **94**, 167401.

55 E. Voloshina, R. Ovcharenko, A. Shulakov and Y. Dedkov, *J. Chem. Phys.*, 2013, **138**, 154706.

56 D. Pacile, M. Papagno, A. F. Rodriguez, M. Grioni, L. Papagno, C. O. Girit, J. C. Meyer, G. E. Begtrup and A. Zettl, *Phys. Rev. Lett.*, 2008, **101**, 066806.

57 M. Weser, Y. Rehder, K. Horn, M. Sicot, M. Fonin, A. B. Preobrajenski, E. N. Voloshina, E. Goering and Y. S. Dedkov, *Appl. Phys. Lett.*, 2010, **96**, 012504.

58 Y. S. Dedkov and M. Fonin, *New J. Phys.*, 2010, **12**, 125004.

59 A. Cabrero-Vilatela, R. S. Weatherup, P. Braeuninger-Weimer, S. Caneva and S. Hofmann, *Nanoscale*, 2015, **8**, 2149–2158.